# Integrated polarization-entangled photon source for wavelength-multiplexed quantum networks

Xiaodong Shi,<sup>1,2,a)</sup> Yue Li,<sup>3,a)</sup> Jinyi Du,<sup>4,a)</sup> Lin Zhou,<sup>3</sup> Ran Yang,<sup>3,5</sup> En Teng Lim,<sup>4,5</sup> Sakthi Sanjeev Mohanraj,<sup>3</sup> Mengyao Zhao,<sup>3</sup> Xu Chen,<sup>3</sup> Xiaojie Wang,<sup>3</sup> Guangxing Wu,<sup>3</sup> Hao Hao,<sup>4</sup> Veerendra Dhyani,<sup>1,2</sup> Sihao Wang,<sup>1,2</sup> Alexander Ling,<sup>4,5,b)</sup> and Di Zhu<sup>3,4,1,2,c)</sup>

<sup>1)</sup> A\*STAR Quantum Innovation Centre (Q.InC), Agency for Science, Technology and Research (A\*STAR), Singapore 138634, Singapore

<sup>2)</sup>Institute of Materials Research and Engineering (IMRE), Agency for Science, Technology and Research (A\*STAR), Singapore 138634, Singapore

<sup>3)</sup>Department of Materials Science and Engineering, National University of Singapore, Singapore 117575, Singapore

<sup>4)</sup>Centre for Quantum Technologies, National University of Singapore, Singapore 117543, Singapore

<sup>5)</sup>Department of Physics, National University of Singapore, Singapore 117551, Singapore

Entangled photons are fundamental resources for quantum communication, computing, and networking. Among them, polarization-entangled photon pairs play an important role due to their straightforward state manipulation and direct use in quantum key distribution, teleportation, and network protocols. However, realizing compact, efficient, and scalable polarization-entangled sources that meet the requirements of practical deployment remains a major challenge. Here, we present a simple yet high-performance on-chip polarization-entangled photon-pair source on thin-film lithium niobate (TFLN). Our device employs dual quasi-phase matching (D-QPM) that sequentially supports type-0 and type-I spontaneous parametric down-conversion in a single nanophotonic waveguide, eliminating the need for interferometers, polarization rotators, or other complex circuits. The source directly produces high-fidelity Bell states with broad bandwidth, high brightness, and low noise. Using this integrated platform, we realize wavelength-multiplexed entanglement distribution in a four-user quantum network deployed over metropolitan fiber links up to 50 km. These results establish a robust and scalable pathway toward practical quantum communication systems and multi-user quantum mesh networks based on integrated photonics.

<sup>&</sup>lt;sup>a)</sup>These authors contributed equally.

b) Electronic mail: alexander.ling@nus.edu.sg

c) Electronic mail: dizhu@nus.edu.sg

## I. INTRODUCTION

Entanglement, a uniquely nonclassical correlation between quantum particles, is a cornerstone of quantum information science and underpins applications ranging from secure communication to quantum computing<sup>1</sup>. Among various forms of entanglement, polarization entanglement plays a central role due to its straightforward state manipulation for direct applications in emerging quantum technologies, such as machine learning on a quantum computer, device-independent quantum key distribution, quantum teleportation, and quantum-enhanced bioimaging<sup>2-14</sup>.

Polarization-entangled photon pairs can be generated through either type-II or type-0/I nonlinear interactions<sup>15</sup>. In type-II spontaneous parametric down-conversion (SPDC), the orthogonal polarizations of signal and idler photons usually have limited phase-matching bandwidth due to polarization-dependent dispersion<sup>16–19</sup>. Traditional type-0/I SPDC in bulk nonlinear crystals avoids these drawbacks, but requires rotation of the pump or the photon-pair polarization, or crystal orientation, often implemented with complex free-space optical setups<sup>20–23</sup>. Such bulky architectures, though historically successful, are intrinsically limited in scalability and not suitable for dense integration.

Recent advances in integrated photonics have sought to overcome these limitations  $^{24,25}$ . Polarization-entangled photon-pair sources have been demonstrated in silicon and silicon nitride platforms via spontaneous four-wave mixing, and in thin-film lithium niobate (TFLN) via type-0 SPDC  $^{26-34}$ . However, these implementations typically rely on auxiliary polarization-handling components, such as polarization beam splitters, polarization rotators, two-dimensional gratings, and cross-polarized dual cavities, which increase system complexity and constrain operational bandwidth. AlGaAs platform exploits both  $\chi^{(2)}$  and  $\chi^{(3)}$  nonlinearities to realize concurrent type-0 and type-I entanglement generation, but they lack flexible and independent control over the two processes  $^{35-37}$ . Thus, despite significant progress, a straightforward, controllable, high-performance, and fully integrated polarization-entangled photon source remains an outstanding challenge.

In this work, we introduce a dual quasi-phase matched (D-QPM) periodically poled lithium niobate (PPLN) nanophotonic waveguide, that directly generates polarization-entangled photon pairs via sequential type-0 and type-I SPDC in a single device. This design eliminates the need for interferometric or polarization-manipulating circuits, while offering flexible and in situ phase-matching control and phase tuning. The source exhibits high brightness, high fidelity, and broadband operation, enabling wavelength-multiplexed entanglement distributions. We further demonstrate long-distance, four-user quantum networking over deployed metropolitan fiber system, underscoring its practicality for real-world quantum communications. Our work provides a simple, compact, robust, and manufacturable pathway for on-chip Bell-state generation, marking an essential step toward practical quantum mesh networks.

#### II. RESULTS

a. Device principle. The D-QPM PPLN nanophotonic waveguide for producing polarization-entangled photon pairs is designed on 600 nm thick x-cut TFLN. Two types of phase matching (type-0 and type-I) can be realized in a single PPLN waveguide with different poling periods (Fig.1a). In type-0 SPDC, a transverse-electric (TE) pump photon converts to a pair of TE signal and idler photons, exploiting the  $\chi^{(2)}$  nonlinear coefficient  $d_{33}^{38}$ .

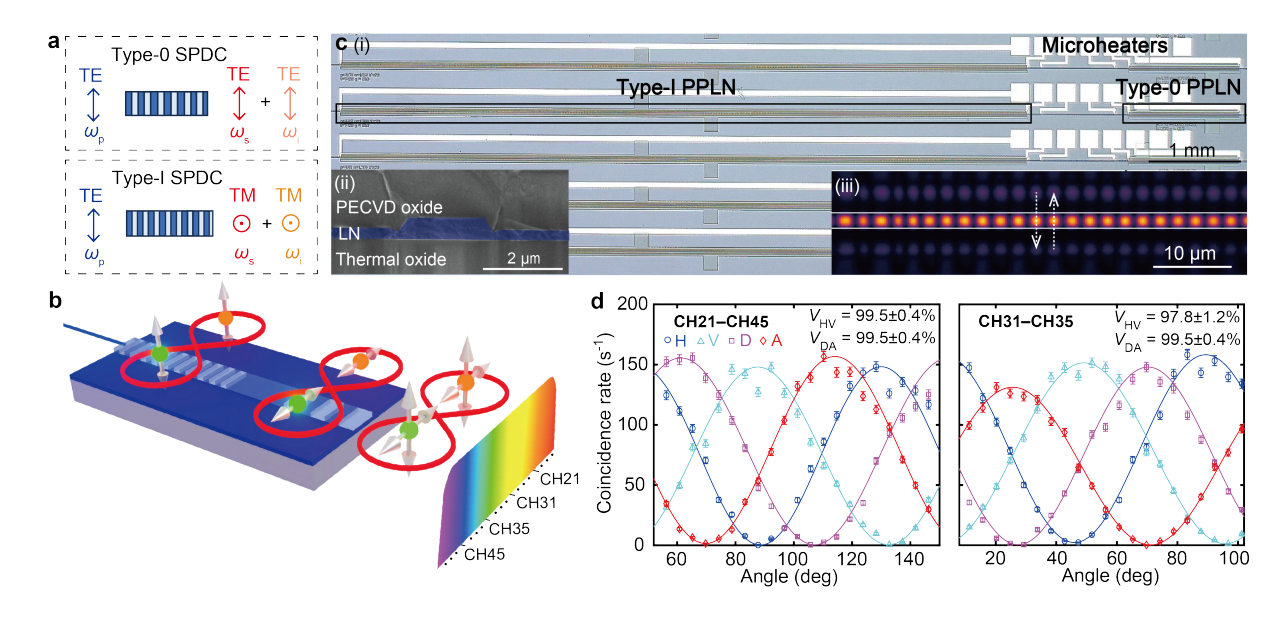


FIG. 1. Dual quasi-phase matching (D-QPM) polarization-entangled photon-pair source in thin-film lithium niobate. a Schematics of type-0 and type-I SPDC in PPLN waveguides with distinct poling periods for phase matching. In type-0 SPDC, a TE pump photon converts to a pair of TE signal and idler photons, while in type-I SPDC, a TE pump photon converts to a pair of TM signal and idler photons. b, Schematic of wavelength-multiplexed polarization-entangled photon-pair source. The device is basically a single straight waveguide incorporating two PPLN sections with distinct poling periods, enabling orthogonally polarized photon-pair generation via type-0 and type-I SPDC. c, (i) Optical micrograph of fabricated D-QPM PPLN waveguide array. Each device integrates two PPLN sections for type-0 and type-I SPDC and three microheaters for independent tuning of their phase-matching wavelengths and relative phase. (ii) False-color cross-sectional scanning electron micrograph of the waveguide. (iii) Laser-scanning SHG imaging of the type-I poled region. d, Two-fold coincidence measurement in H, V, D, and A bases for far non-degenerate (CH21-CH45) and near-degenerate (CH31-CH35) photon pairs, respectively. Raw visibilities are measured to be >97% without accidental subtraction, confirming high-quality polarization-entangled photon-pair source.

While in type-I SPDC, a TE pump photon converts to a pair of transverse-magnetic (TM) signal and idler photons, leveraging  $d_{31}$ . The core device to produce polarization-entangled photon pairs on TFLN is basically a single straight LN nanophotonic waveguide comprising two sequentially arranged sections of PPLN, each engineered with a distinct poling period (Fig.1b). One PPLN section is designed for type-0 quasi-phase matching (QPM) between the fundamental-harmonic (FH) TE mode and the second-harmonic (SH) TE mode. The other section supports type-I QPM between the FH TM mode and SH TE mode.

When the dual-QPM PPLN device is pumped at the SH wavelength, both type-0 and type-I SPDC processes occur sequentially, generating TE-polarized ( $|H_sH_i\rangle$ ) and TM-polarized ( $|V_sV_i\rangle$ ) photon pairs around the FH wavelength, respectively. The resulting polarization-entangled state at the waveguide output can be expressed as  $|\psi\rangle = \alpha |H_sH_i\rangle + \beta e^{i\phi}|V_sV_i\rangle$ , where  $\alpha$  and  $\beta$  are the probability amplitudes of the two SPDC processes, and  $\phi$  represents their relative phase. Maximal entanglement is obtained when  $\alpha = \beta$  and  $\phi = 0$  or  $\pi$ , yielding  $|\psi_{max}\rangle = \frac{1}{\sqrt{2}}(|H_sH_i\rangle \pm |V_sV_i\rangle)$ . To achieve the conditions,

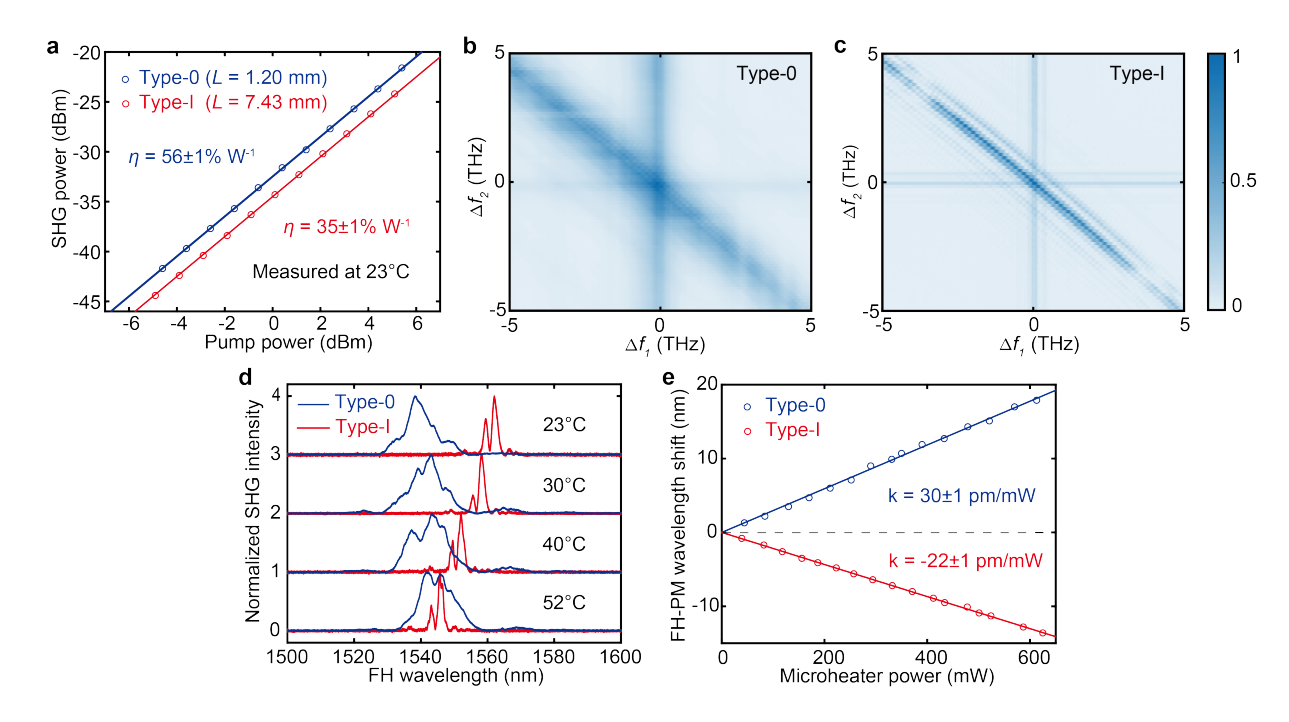


FIG. 2. Classical characterization of D-QPM PPLN waveguide. a, Measured type-0 (blue circles) and type-I (red circles) on-chip SHG power as a function of pump power, and linear fits (lines) yield conversion efficiencies of  $56 \pm 1\%$  and  $35 \pm 1\%$ , respectively. b, c, Sum-frequency generation spectra for type-0 and type-I PPLN waveguides. The anti-diagonal features indicate broadband phase matching for both SPDC processes. d, Type-0 (blue) and type-I (red) SHG spectra at different chip temperatures. The type-0 spectrum red shifts, whereas type-I blue shifts with increasing temperature. The phase-matching wavelength difference between type-0 and type-I PPLNs can be compensated through thermal tuning. e, Fundamental-harmonic (FH) phase-matching (PM) wavelength as a function of applied microheater power for type-0 (blue) and type-I (red) SHG. Wavelength shifts of  $30 \pm 1$  pm mW<sup>-1</sup> (type-0) and  $-22 \pm 1$  pm mW<sup>-1</sup> (type-I) demonstrate independently efficient thermal tuning of each PPLN section.

we tailor the lengths of each PPLN section to balance pair generation rates and introduce a thermo-optic phase shifter between them to fine-tune the relative phase.

The D-QPM PPLN devices are fabricated (Fig.1c, see Materials and Methods for fabrication details). The type-0 PPLN section is 1.20 mm long with a poling period of 4.76 µm, while the type-I section is 7.43 mm long with a poling period of 4.54 µm. The lengths are designed according to their nonlinear strengths to ensure identical pair generation rates, and the poling periods are calculated based on type-0/I QPM conditions (see Materials and Methods for design details). Integrated microheaters, positioned above each PPLN region and in between, enable independent tuning of the QPM wavelengths and relative phase, respectively.

To demonstrate polarization entanglement, we balance the pair generation rates from the two types of SPDC in the D-QPM PPLN device via thermal tuning. The generated photons are spectrally separated via external dense wavelength division multiplexing (DWDM) channels. Two representative wavelength channel pairs are chosen for polarization entanglement measurements: one far non-degenerate pair (CH21–CH45) and one near-degenerate pair (CH31–CH35) (Fig.1d). The high visibilities indicate that the proposed architecture

produces high-fidelity polarization-entangled photon pairs.

b. Classical characterization of D-QPM PPLN waveguide. The device's classical performance is evaluated through second-harmonic generation (SHG) and sum-frequency generation (SFG) measurements. The SHG conversion efficiencies of the type-0 and type-I PPLN waveguides are obtained by continuous-wave (CW) pumping at their respective phase-matched (PM) FH wavelengths with TE and TM polarizations at room temperature, respectively (Fig.2a). The measured normalized conversion efficiencies are  $56.5 \pm 0.8\% \text{ W}^{-1}$  for type-0 and  $35.5 \pm 0.7\% \text{ W}^{-1}$  for type-I, with the difference attributed to fabrication imperfections such as variations in poling depth, duty cycle, and thin-film thickness. The PM characteristics are further examined via SFG measurements (Figs.2b, c). The anti-diagonal slopes of both PPLN follow the energy conservation line ( $\Delta f_1 + \Delta f_2 = 0$ ), indicative of broadband SPDC.

The measured PM wavelengths slightly deviate from the design due to fabrication fluctuations. To compensate for these shifts, we characterize the thermal response of the PPLN PM wavelengths. As the chip temperature increases, the type-0 SHG spectrum red shifts, whereas the type-I spectrum blue shifts (Fig.2d). Thus, alignment of the two PM wavelengths can be achieved by increasing the temperature. Individual PM wavelength adjustments are performed by applying electrical power to the integrated microheater on top of each PPLN section. The FH PM wavelength shifts by  $30 \pm 1$  pm mW<sup>-1</sup> for type-0 and  $-22 \pm 1$  pm mW<sup>-1</sup> for type-I SHG (Fig.2e). This flexible and independent on-chip thermal control on the PM wavelengths of the two PPLN sections also enables precise balancing of the pair generation rates from the type-0 and type-I SPDC processes, a critical requirement for achieving high-fidelity polarization-entangled states.

c. Non-classical characterization of D-QPM PPLN waveguide. We next balance the type-0 and type-I SPDC rates through thermal tuning and characterize their non-classical performances separately before evaluating polarization entanglement (Fig.3a, see Materials and Methods for experimental details). We measure the pair generation rate and coincidence-to-accidental ratio (CAR) as a function of pump power from a randomly chosen channel pair (CH21-CH45) (Fig.3b, c). For type-0 SPDC, the measured pair efficiency is  $(2.6\pm0.1)\times10^3$  s<sup>-1</sup>mW<sup>-1</sup>, corresponding to an inferred on-chip efficiency of  $2.1\times10^7$  s<sup>-1</sup>mW<sup>-1</sup>. For type-I SPDC, the measured efficiency is  $(2.5\pm0.1)\times10^3$  s<sup>-1</sup>mW<sup>-1</sup>, yielding an on-chip efficiency of  $2.0\times10^7$  s<sup>-1</sup>mW<sup>-1</sup>. Considering the 0.3 nm DWDM channel bandwidth, the source brightness is  $\sim6.7\times10^7$  s<sup>-1</sup>mW<sup>-1</sup>nm<sup>-1</sup>. The CARs are above  $5\times10^2$  across all measurements and exceed  $5\times10^3$  at pump powers below 0.03 mW for both SPDC.

Heralded second-order correlations  $(g_H^{(2)}(\tau))$  are measured by splitting photons in CH45 and detecting multi-photon events (Fig.3a(iv)). The measured  $g_H^{(2)}(\tau)$  at zero time delay  $(g_H^{(2)}(0))$  for type-0 and type-I SPDC are both below 0.01 at 0.63 mW pump power (Fig.3d, e), confirming operation deep in the single-photon regime.

Joint spectral intensities (JSI) are reconstructed using 32 DWDM channels (CH17 to CH32 and CH49 to CH34) (Fig.3f, g). The JSI for type-0 and type-I SPDC shows flat pair generation rates across 16 telecom C-band channel pairs with <10% coincidence variation. The strong frequency correlations over multiple wavelength channels highlight the potential of the source for wavelength-multiplexed quantum applications.

d. Polarization entanglement measurements. After balancing and characterizing the type-0 and type-I SPDC photon-pair sources, we verify the polarization entanglement of the source. The generated photons (Fig.3a) are spectrally separated via DWDM channels (Fig.4c). Two representative channel pairs are randomly chosen for polarization-

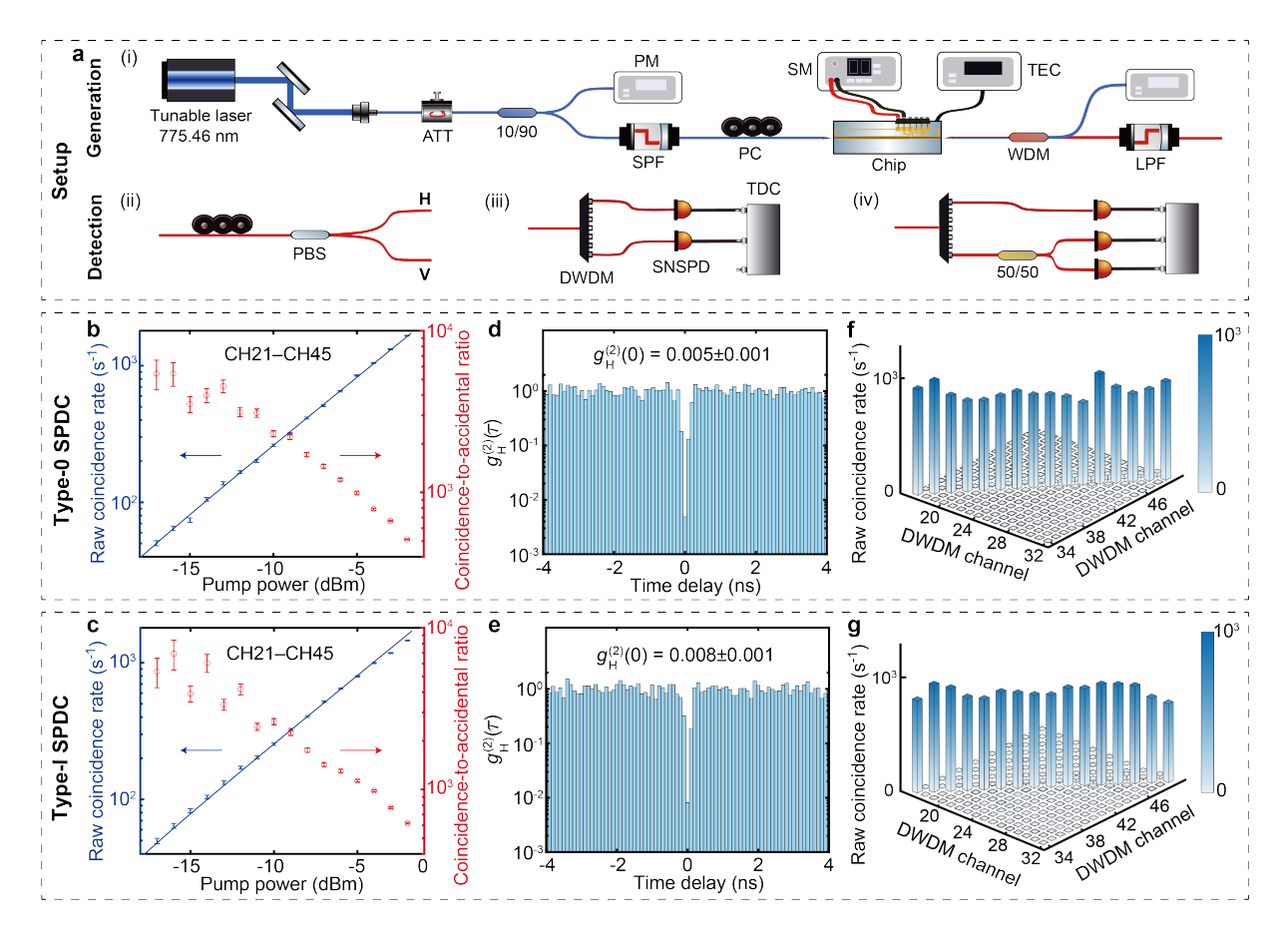


FIG. 3. Non-classical characterization of D-QPM PPLN photon-pair source. a, Experimental setup for (i) polarization-entangled photon-pair generation, (ii) separation of type-0 (H) and type-I (V) photon pairs, (iii) measurement of wavelength-multiplexed pair generation rate and coincidence-to-accidental ratio (CAR), and (iv) measurement of heralded second-order correlation. ATT: tunable attenuator, 10/90: 10/90 beam splitter; PM: power meter; SPF: short-pass filter; PC: polarization controller; SM: source meter; TEC: thermoelectric cooling; WDM: 1550 nm/775 nm wavelength division multiplexer; LPF: long-pass filter; PBS: polarization beam splitter; DWDM: dense wavelength division multiplexer; SNSPD: superconducting nanowire single-photon detector; TDC: time-to-digital converter; 50/50: 50/50 beam splitter. b, c, Measured raw coincidence counts (blue dots) and quadratic fits (blue line) for type-0 and type-I SPDC, along with CAR (red) as a function of pump power, using selected channel pair CH21-CH45. d, e, Heralded second-order correlation function for type-0 and type-I SPDC at 0.63 mW pump power. Values below 0.01 at zero time delay confirm single-photon operation. f, g, Joint spectral intensity of type-0 and type-I SPDC, reconstructed from correlations across 32 DWDM channels (CH17 to CH32 and CH49 to CH34). The results demonstrate broadband operation with strong frequency correlations.

entanglement measurements: one far non-degenerate pair (CH21–CH45) and one near-degenerate pair (CH31–CH35) (Fig.1d). Each pair is measured in horizontal (H), vertical (V), diagonal (D), and anti-diagonal (A) bases. Two-fold coincidence for the two pairs is measured with raw visibilities of  $V_{\rm H/V}=99.5\pm0.4\%$  and  $V_{\rm D/A}=99.5\pm0.4\%$  for CH21–CH45, and  $V_{\rm H/V}=97.8\pm1.2\%$  and  $V_{\rm D/A}=99.5\pm0.4\%$  for CH31–CH35, without accidental subtraction. The results exhibit sinusoidal curves with constructive and destructive interference,

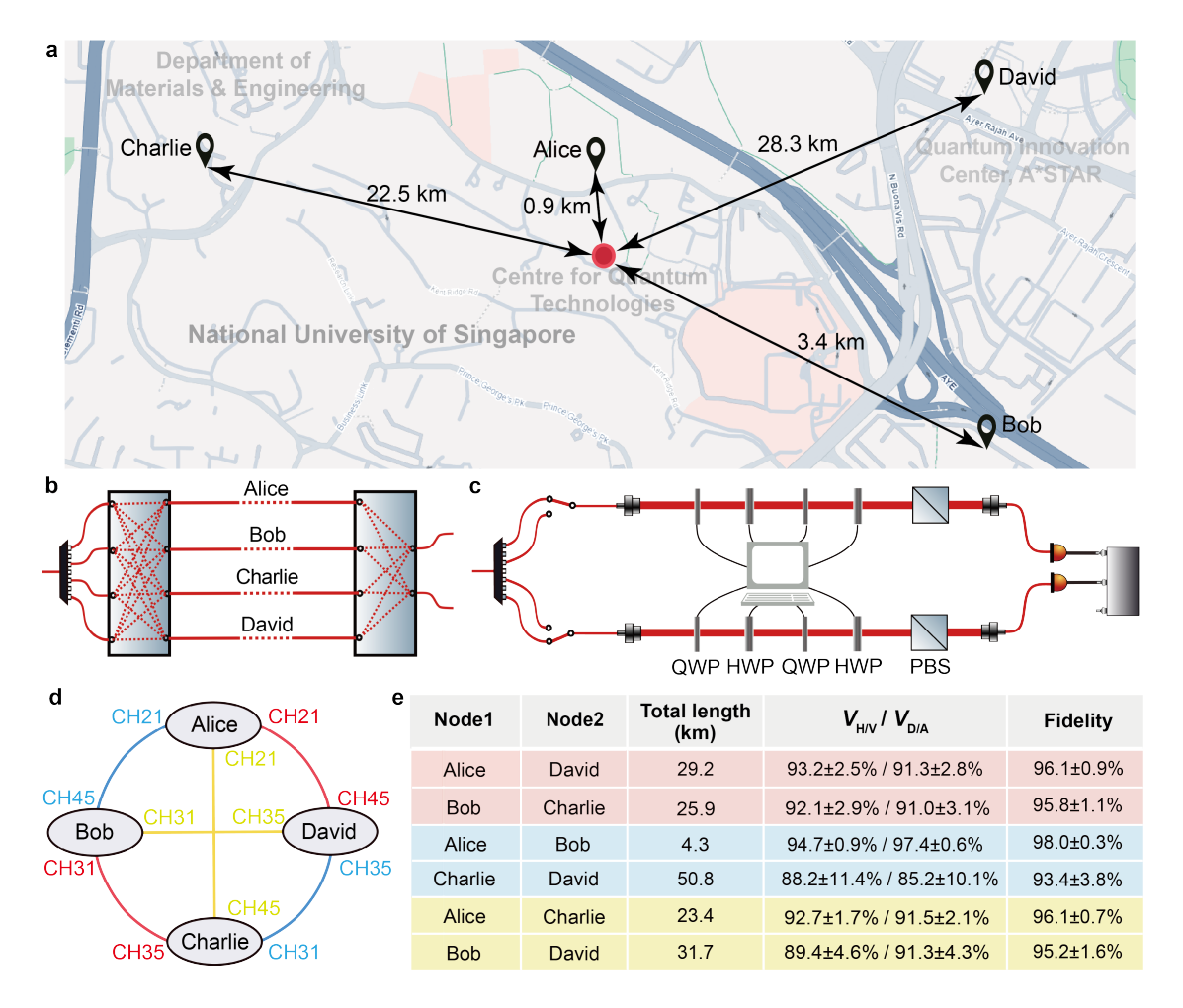


FIG. 4. Long-distance multi-user entanglement demonstration over deployed metropolitan optical fibers. a, Map of the deployed optical fiber network used to realize a four-user wavelength-multiplexed quantum network (Map date from Google Earth). b, Schematic of network operation, where entangled photons from two DWDM channel pairs are distributed to four nodes (Alice, Bob, Charlie, and David), and looped back for detection. The loopback deployed fiber lengths are 0.9 km, 3.4 km, 28.3 km, and 22.5 km, respectively. Note that these lengths differ from the geographical distances shown on the map due to the practical routing of the deployed fiber network. c, Experimental setup for polarization-entanglement measurements. QWP: quarter-wave plate; HWP: half-wave plate. d, Communication layer of the quantum mesh network. Each user is fully connected to all others via three wavelength-distribution configurations (red, blue, and yellow) using two DWDM channel pairs (CH21–CH45 and CH31–CH35). e, Measured raw visibilities for all two-user connections without accidental subtraction, demonstrating robust polarization entanglement across long-distance fiber links up to 50 km.

confirming the quantum correlations between the signal and idler photons. The corresponding Bell-state fidelities are estimated to be  $99.8 \pm 0.1\%$  and  $99.3 \pm 0.3\%$ , close to an ideal Bell state<sup>39,40</sup>.

To demonstrate the source's suitability for long-distance multi-user quantum networks, entangled photons are distributed over deployed metropolitan optical fibers (provided by National Quantum-Safe Network) connecting four locations across Singapore (labeled as

Alice, Bob, Charlie, and David), and looped back for detection (Fig.4a-c). Concurrently using two DWDM channel pairs (CH21–CH45 and CH31–CH35), we configure three combinations (red, blue, and yellow) to realize a four-user quantum network (Fig.4d). Taking the red combination as an example, CH21–CH45 are distributed to Alice and David paths, while CH31–CH35 are distributed to Bob and Charlie paths, for entanglement distribution between each pair of nodes. Raw visibilities for each combination, as well as the total link distances, are summarized (Fig.4e). For instance, when CH21–CH45 are sent to Alice and David (29.2 km) and CH31–CH35 to Bod and Charlie (25.9 km), the measured visibilities are  $V_{\rm H/V} = 93.2 \pm 2.5\%$ ,  $V_{\rm D/A} = 91.3 \pm 2.8\%$  and  $V_{\rm H/V} = 92.1 \pm 2.9\%$ ,  $V_{\rm D/A} = 91.0 \pm 3.1\%$ , corresponding to fidelities of 96.1±0.9% and 95.8±1.1%, respectively. Similar measurements for the other combinations yield fidelities ranging from 93% to 98%. All measured visibilities far exceed the 70.7% threshold for violating CHSH inequality, and the overall good fidelities indicate the robustness of the source for some practical quantum applications, such as entanglement swapping and entanglement-based QKD protocols<sup>41–46</sup>.

### III. DISCUSSION

There remain several avenues for improving both device performances and its applications in quantum networks. The relatively low raw pair rates observed in the measurements, compared with the intrinsic source brightness, are limited by the insertion loss of fiber systems, as well as the chip-to-fiber coupling loss. Incorporating more efficient coupling schemes, such as trident edge couplers or SU8 tapers, could reduce this bottleneck<sup>47,48</sup>.

The fidelity of entanglement distribution through deployed fiber networks is found to decrease relative to direct source measurements. The degradation primarily arises from accumulated polarization-mode dispersion (PMD) in the long-distance fibers, which distorts the polarization states of the entangled photons<sup>49</sup>. In our network demonstration, a loop-back configuration is used, effectively doubling the optical path length between nodes. As a result, the fiber loss and PMD are twice those expected in an actual network, and the fidelities reported here represent conservative estimates of real-world performance. Implementing active polarization stabilization or advanced compensation strategies could mitigate the PMD effect and maintain high-fidelity transmission over extended distances<sup>50</sup>. Alternatively, narrowing the photon-pair spectral bandwidth, for instance, by employing microring resonators that generate ultra-bright, narrow-band photon pairs, can further suppress the impacts of both PMD and chromatic dispersion<sup>51</sup>. These approaches will collectively enhance the robustness and scalability of entanglement distribution for practical quantum network deployment.

Our current network demonstration distributes entanglement among four nodes, and relies on reusing wavelength channels. Leveraging the broadband operation of our polarization-entangled photon-pair source (Fig.3f, g) would allow full utilization of available DWDM channels across the telecom C-band, thereby enabling simultaneous entanglement distribution among more users. This scalability is crucial for realizing high-capacity quantum networks. Distributed detectors can be implemented at each node to achieve a fully functional quantum mesh network, where independent users can simultaneously share and verify entanglement across the network<sup>52</sup>.

More broadly, our integrated D-QPM PPLN architecture provides a simple and scalable solution for on-chip generation of Bell states. By sequentially implementing type-0 and type-I SPDC, and balancing their contributions via integrated microheaters, the device

produces high-fidelity polarization entanglement without the need for external polarization components or interferometric schemes. The combination of high brightness, broadband tunability, and robust polarization control supports multi-channel entanglement distribution and positions this source as a strong candidate for networked quantum technologies. Looking ahead, integrating pump sources and detectors on chip, as well as hybrid interfacing with quantum memories, could yield a multifunctional and fully integrated entanglement node. Such advances would not only benefit terrestrial fiber networks but also enable deployment in space-based quantum communication systems, where compactness, efficiency, and robustness are paramount<sup>53,54</sup>.

### MATERIALS AND METHODS

- a. Device design. The D-QPM PPLN nanophotonic waveguide is designed along the crystal y-axis on a 600 nm thick x-cut TFLN integrated platform. The waveguide has a width of 2 µm with an etching depth of 300 nm. The poling periods for type-0 and type-I QPM process is calculated to be 4.76 µm and 4.54 µm, according to  $\Lambda = \frac{\lambda_{\rm FH}}{2(n_{\rm SH}-n_{\rm FH})}$ , where  $\lambda_{\rm FH}$  is the FH wavelength (1550 nm) and  $n_{\rm SH/FH}$  is the corresponding effective index of the involved SH/FH modes. We evaluate the nonlinear efficiency of the type-0 and type-I QPM processes based on the SHG conversion efficiency,  $\eta = \frac{8\pi^2}{\epsilon_0 c n_{\rm FH}^2 n_{\rm SH} \lambda_{\rm FH}^2} d_{\rm eff}^2 \Gamma L^2$ , where  $\epsilon_0$  is the free-space permittivity, c is the speed of light,  $d_{\rm eff}$  is the effective  $\chi^{(2)}$  coefficient ( $d_{\rm eff} = \frac{2}{\pi} d_{33}$  for type-0 and  $d_{\rm eff} = \frac{2}{\pi} d_{31}$  for type-I phase-matching processes), and L is the length of the phase-matched waveguide<sup>55</sup>.  $\Gamma$  is the nonlinear coupling parameter between the FH and SH modes, given by  $\Gamma = \frac{|\int_{\rm LN} (E_{\pi/z,{\rm FH}})^2 E_{z,{\rm SH}} dz dz|^2}{|\int_{\rm all} |E_{\rm FH}|^2 dx dz|^2 \int_{\rm all} |E_{\rm SH}|^2 dx dz}$ . Here, we only consider the overlap of the x and z-components of the electric fields (E) for the TM and TE modes, respectively. To match the nonlinear strength of the type-I and type-0 phase-matching process, the ratio of the corresponding PPLN lengths is  $\sim 6.19$ , so we choose 7.43 mm and 1.20 mm, respectively, in the experiment.
- b. Device fabrication. We fabricate the D-QPM PPLN device in a 600 nm thick MgO-doped x-cut TFLN chip (NanoLN). A 15 nm thick HfO<sub>2</sub> layer is deposited on TFLN using atomic-layer deposition (ALD) as a buffer layer for electrical poling. The comb-like electrode is patterned, using e-beam lithography, e-beam metal evaporation (60 nm Ni and 60 nm Cr) and lift-off. We apply a series of electrical pulses to periodically reverse the polarity in the LN thin film. The waveguides are patterned using e-beam lithography and Ar<sup>+</sup> etching by inductively coupled plasma reactive ion etching (ICP-RIE), with MaN e-beam resist as the etching mask. A 1.6 μm thick silicon dioxide thin film is then deposited on top of the waveguide by plasma-enhanced chemical vapor deposition (PECVD). The thermal microheater is finally patterned, using ultraviolet lithography, e-beam metal evaporation (90 nm Pt) and lift-off. Overview of fabricated device array, scanning electron micrograph of waveguide cross section, and top-view laser-scanning SHG imaging of the poled waveguide are shown in Fig.1c.
- c. Experimental details for classical characterizations of D-QPM PPLN waveguide. To extract the type-0 and type-I SHG conversion efficiencies, we first calibrate the fiber-to-chip coupling loss using lensed fibers, and the coupling losses are measured to be 5.4 dB per facet for TE polarization and 5.7 dB per facet for TM polarization around 1550 nm, and 8.7 dB per facet for TE polarization around 775 nm. Polarizations are aligned with a fiber polarization controller (PC) and verified using an infrared polarimeter before coupling into

the waveguide. For Fig.2a, the CW pump laser (Santec TSL-570) is fixed at the phase-matching wavelength of type-0 and type-I SHG (room temperature), while the pump power is swept and the SHG output is measured with an infrared power meter. Both pump and SHG powers are referenced on-chip. For Fig.2b, c, two tunable telecom CW lasers are synchronously swept around the phase-matching wavelengths, combined, and coupled into the waveguide to record the generated SFG power with a data acquisition system. For Fig.2d, SHG spectra at different temperatures are obtained by synchronously sweeping a telecom CW laser and monitoring the SHG power with a data acquisition system, while the chip stage temperature is stabilized using a TEC module. For Fig.2e, DC bias is applied to the integrated microheaters via electrical probes using a source meter, and the corresponding phase-matching wavelength shifts are recorded.

- Experimental details for non-classical characterizations of D-QPM PPLN wavequide. We use the experimental setups shown in Fig. 3a to characterize the individual type-0 and type-I SPDC processes in the device. Figure 3a(i) illustrates the setup for polarizationentangled photon-pair preparation. A tunable CW laser at 775.46 nm, corresponding to ITU channel CH33 at its FH wavelength, is used as the pump. The pump is coupled into optical fiber via a collimator, with its power controlled by a tunable attenuator and monitored by a power meter through a 10/90 beam splitter. Pump noise is suppressed using a short-pass filter, and the polarization is adjusted to TE with a PC before launching into the waveguide. After type-0 and type-I SPDC in the PPLN sections, the pump and photon pairs are collected with a lensed fiber and separated by a 775/1550 nm WDM. The residual pump is monitored by a power meter, while the photon pairs are passed through a long-pass filter to suppress pump leakage and Raman noise. TE and TM photons are then separated using a PC and polarization beam splitter (PBS) (Fig. 3a(ii)). Polarization alignment is verified using SHG from calibrated pump inputs. To balance the type-0 and type-I pair generation rates, a 15 nm bandpass filter centered at 1550 nm is initially inserted, ensuring equivalent collection of broad bandwidths. Each PBS output is further divided by a 50/50 beam splitter and detected by SNSPDs, with coincidences recorded on a time-to-digital converter (TDC). By thermally tuning the device and monitoring coincidence rates, the two SPDC processes are balanced. The bandpass filter is then removed, and PBS outputs are routed through DWDM modules to select channel pairs (CH21-CH45) for individual type-0 and type-I measurements (Fig.3a(iii)). Coincidence countings (Fig.3b, c, f, g) are measured using these setups. For heralded second-order correlation  $(g_H^{(2)})$  measurements (Fig.3d, e), CH45 is split by a 50/50 beam splitter, and both outputs are detected by SNSPDs together with heralded CH21 photons (Fig. 3a(iv)). A virtual delay  $((\tau))$  is introduced in one of the split arms using the time tagger to extract  $(g_H^{(2)}(\tau))$ .
- e. Experimental details for polarization entanglement measurements. To characterize polarization entanglement, the source output (Fig.3a(i)) is connected to the detection setup (Fig.4c). The generated photon pairs are separated by a DWDM module, and photons from the selected channel pairs are directed into two free-space arms. Each arm passes through a sequence of QWP-HWP-QWP to compensate for fiber birefringence, followed by a HWP and PBS for polarization state projection. The wave plates are mounted on motorized rotation stages under programmable electrical control, enabling automated polarization scanning. The second HWP in the upper arm is fixed at an angle corresponding to one of H, V, D, and A bases, while the HWP in the bottom arm is rotated over 90°, which projects the entangled photons into the specific polarization base. The projected photons are then coupled back into fibers and detected by SNSPDs for coincidence counting. Polariza-

tion entanglement measurements are conducted for selected channel pairs CH31–CH35 and CH21–CH45 (Fig.1d). These are chosen to show that both nearly degenerate and far non-degenerate photon pairs work for this wavelength-multiplexed source. Other channel pairs could also work as well. For long-distance multi-user entanglement measurement (Fig.4e), after wavelength demultiplexing, two selected channel pairs (CH31–CH35, CH21–CH45) are distributed into four deployed optical fiber links, named Alice, Bob, Charlie, and David (Fig.4b), according to the communication layer (Fig.4d). Each path is then looped back for polarization analysis and detection. Deployed metropolitan fiber loop lengths for Alice, Bob, Charlie, and David paths are 0.9 km, 3.4 km, 28.3 km, and 22.4 km. For the longest-distance measurement between Charlie and David (50.8 km), a 40 km dispersion compensation module is added to the David path before detection, to compensate for the accumulated dispersion of ~650 ps nm<sup>-1</sup>.

#### ACKNOWLEDGEMENTS

The authors thank Jing Yan Haw, Hao Qin, and Matthew Wee for providing access to the deployed fiber infrastructure, and Christian Kurtsiefer and Hou Shun Poh for their valuable advice on quantum networks. The authors also acknowledge Netlink Trust for provisioning the fiber network used in this work. This research was supported by National Research Foundation, Singapore (NRF-NRFF15-2023-0005, W24Q3D0001), Singapore Ministry of Education (MOET32024-0009), A\*STAR (M23M7c0125), and Centre for Quantum Technologies Funding Initiative (S24Q2d0009).

### COMPETING INTERESTS

The authors declare no competing interests.

# CONTRIBUTIONS

D.Z., A.L., X.S., Y.L., and J.D. conceived the idea. X.S. and Y.L. designed the devices. Y.L., S.S.M., X.C., H.H, and V.D. fabricated the devices. X.S., Y.L., J.D., L.Z., R.Y., M.Z., X.W., G.W., and S.W. performed the classical and non-classical measurements of the devices. J.D., X.S., Y.L., and E.T.L. performed the entanglement and network measurements. D.Z. and A.L. supervised the project. All the authors discussed the results and wrote the manuscript.

#### REFERENCES

<sup>&</sup>lt;sup>1</sup>R. Horodecki, P. Horodecki, M. Horodecki, and K. Horodecki, "Quantum entanglement," Reviews of Modern Physics **81**, 865–942 (2009).

<sup>&</sup>lt;sup>2</sup>X.-D. Cai, D. Wu, Z.-E. Su, M.-C. Chen, X.-L. Wang, L. Li, N.-L. Liu, C.-Y. Lu, and J.-W. Pan, "Entanglement-based machine learning on a quantum computer," Physical Review Letters **114**, 110504 (2015).

- <sup>3</sup>Z. Zhang, C. You, O. S. Magaña-Loaiza, R. Fickler, R. d. J. León-Montiel, J. P. Torres, T. S. Humble, S. Liu, Y. Xia, and Q. Zhuang, "Entanglement-based quantum information technology: a tutorial," Advances in Optics and Photonics **16**, 60–162 (2024).
- <sup>4</sup>S. Wengerowsky, S. K. Joshi, F. Steinlechner, H. Hübel, and R. Ursin, "An entanglement-based wavelength-multiplexed quantum communication network," Nature **564**, 225–228 (2018).
- <sup>5</sup>J. Yin, Y.-H. Li, S.-K. Liao, M. Yang, Y. Cao, L. Zhang, J.-G. Ren, W.-Q. Cai, W.-Y. Liu, S.-L. Li, et al., "Entanglement-based secure quantum cryptography over 1,120 kilometres," Nature **582**, 501–505 (2020).
- <sup>6</sup>D. Bouwmeester, J.-W. Pan, K. Mattle, M. Eibl, H. Weinfurter, and A. Zeilinger, "Experimental quantum teleportation," Nature **390**, 575–579 (1997).
- <sup>7</sup>J. Yin, Y. Cao, Y.-H. Li, S.-K. Liao, L. Zhang, J.-G. Ren, W.-Q. Cai, W.-Y. Liu, B. Li, H. Dai, et al., "Satellite-based entanglement distribution over 1200 kilometers," Science **356**, 1140–1144 (2017).
- <sup>8</sup>A. N. Craddock, A. Lazenby, G. B. Portmann, R. Sekelsky, M. Flament, and M. Namazi, "Automated distribution of polarization-entangled photons using deployed new york city fibers," PRX Quantum 5, 030330 (2024).
- <sup>9</sup>S. Wengerowsky, S. K. Joshi, F. Steinlechner, J. R. Zichi, S. M. Dobrovolskiy, R. Van der Molen, J. W. Los, V. Zwiller, M. A. Versteegh, A. Mura, *et al.*, "Entanglement distribution over a 96-km-long submarine optical fiber," Proceedings of the National Academy of Sciences **116**, 6684–6688 (2019).
- <sup>10</sup>R. Ursin, F. Tiefenbacher, T. Schmitt-Manderbach, H. Weier, T. Scheidl, M. Lindenthal, B. Blauensteiner, T. Jennewein, J. Perdigues, P. Trojek, et al., "Entanglement-based quantum communication over 144 km," Nature Physics 3, 481–486 (2007).
- <sup>11</sup>J. Yin, J.-G. Ren, H. Lu, Y. Cao, H.-L. Yong, Y.-P. Wu, C. Liu, S.-K. Liao, F. Zhou, Y. Jiang, et al., "Quantum teleportation and entanglement distribution over 100-kilometre free-space channels," Nature 488, 185–188 (2012).
- <sup>12</sup>X.-S. Ma, T. Herbst, T. Scheidl, D. Wang, S. Kropatschek, W. Naylor, B. Wittmann, A. Mech, J. Kofler, E. Anisimova, et al., "Quantum teleportation over 143 kilometres using active feed-forward," Nature 489, 269–273 (2012).
- <sup>13</sup>Y.-A. Chen, Q. Zhang, T.-Y. Chen, W.-Q. Cai, S.-K. Liao, J. Zhang, K. Chen, J. Yin, J.-G. Ren, Z. Chen, et al., "An integrated space-to-ground quantum communication network over 4,600 kilometres," Nature 589, 214–219 (2021).
- <sup>14</sup>Y. Zhang, Z. He, X. Tong, D. C. Garrett, R. Cao, and L. V. Wang, "Quantum imaging of biological organisms through spatial and polarization entanglement," Science Advances 10, eadk1495 (2024).
- <sup>15</sup>A. Anwar, C. Perumangatt, F. Steinlechner, T. Jennewein, and A. Ling, "Entangled photon-pair sources based on three-wave mixing in bulk crystals," Review of Scientific Instruments **92** (2021).
- <sup>16</sup>P. G. Kwiat, K. Mattle, H. Weinfurter, A. Zeilinger, A. V. Sergienko, and Y. Shih, "New high-intensity source of polarization-entangled photon pairs," Physical Review Letters 75, 4337 (1995).
- <sup>17</sup>P. Trojek, C. Schmid, M. Bourennane, H. Weinfurter, and C. Kurtsiefer, "Compact source of polarization-entangled photon pairs," Optics express **12**, 276–281 (2004).
- <sup>18</sup>C.-W. Sun, S.-H. Wu, J.-C. Duan, J.-W. Zhou, J.-L. Xia, P. Xu, Z. Xie, Y.-X. Gong, and S.-N. Zhu, "Compact polarization-entangled photon-pair source based on a dual-periodically-poled ti: Linbo3 waveguide," Optics letters 44, 5598–5601 (2019).

- <sup>19</sup>A. Martin, A. Issautier, H. Herrmann, W. Sohler, D. B. Ostrowsky, O. Alibart, and S. Tanzilli, "A polarization entangled photon-pair source based on a type-ii ppln waveguide emitting at a telecom wavelength," New Journal of Physics 12, 103005 (2010).
- <sup>20</sup>P. G. Kwiat, E. Waks, A. G. White, I. Appelbaum, and P. H. Eberhard, "Ultrabright source of polarization-entangled photons," Physical Review A **60**, R773 (1999).
- <sup>21</sup>M. Jabir and G. K. Samanta, "Robust, high brightness, degenerate entangled photon source at room temperature," Scientific reports **7**, 12613 (2017).
- <sup>22</sup>H. Terashima, S. Kobayashi, T. Tsubakiyama, and K. Sanaka, "Quantum interferometric generation of polarization entangled photons," Scientific reports 8, 15733 (2018).
- <sup>23</sup>A. Lohrmann, C. Perumangatt, A. Villar, and A. Ling, "Broadband pumped polarization entangled photon-pair source in a linear beam displacement interferometer," Applied Physics Letters **116** (2020).
- <sup>24</sup>A. Orieux, M. A. Versteegh, K. D. Jöns, and S. Ducci, "Semiconductor devices for entangled photon pair generation: a review," Reports on Progress in Physics 80, 076001 (2017).
- <sup>25</sup>S. Signorini and L. Pavesi, "On-chip heralded single photon sources," AVS Quantum Science **2** (2020).
- <sup>26</sup>Z. Jiang, W. Yan, C. Lu, Y. Chen, W. Wen, Y.-Y. An, L. Chen, Y. Lu, S. Zhu, and X.-S. Ma, "Entanglement distribution over metropolitan fiber using on-chip broadband polarization entangled photon source," arXiv preprint arXiv:2503.07198 (2025).
- <sup>27</sup>J. Du, X. Zhang, G. F. Chen, H. Gao, D. T. Tan, and A. Ling, "Demonstration of entanglement distribution over 155 km metropolitan fiber using a silicon nanophotonic chip," arXiv preprint arXiv:2409.17558 (2024).
- <sup>28</sup>N. Matsuda, H. Le Jeannic, H. Fukuda, T. Tsuchizawa, W. J. Munro, K. Shimizu, K. Yamada, Y. Tokura, and H. Takesue, "A monolithically integrated polarization entangled photon pair source on a silicon chip," Scientific Reports 2, 817 (2012).
- <sup>29</sup>N. Lv, W. Zhang, Y. Guo, Q. Zhou, Y. Huang, and J. Peng, "1.5  $\mu$ m polarization entanglement generation based on birefringence in silicon wire waveguides," Optics Letters **38**, 2873–2876 (2013).
- <sup>30</sup>L. Olislager, J. Safioui, S. Clemmen, K. P. Huy, W. Bogaerts, R. Baets, P. Emplit, and S. Massar, "Silicon-on-insulator integrated source of polarization-entangled photons," Optics Letters 38, 1960–1962 (2013).
- <sup>31</sup>Q. Zhang, K. Wu, and A. W. Poon, "Polarization entanglement generation in silicon nitride waveguide-coupled dual microring resonators," Optics Express **32**, 22804–22816 (2024).
- <sup>32</sup>X. Hua, X. Yan, L. Xu, Y. Zhu, M. Liu, J. Yan, D. Chen, H. Zhang, and X. Xiao, "A bright polarization-entangled photon pair source based on silicon photonics integration," APL Photonics **10** (2025).
- <sup>33</sup>C. Kim, H. Kim, M. Choi, J. Lee, Y. Park, S. Moon, J. Lee, H. Hwang, M.-K. Seo, Y.-H. Kim, et al., "Integrated bright source of polarization-entangled photons using lithium niobate photonic chips," arXiv preprint arXiv:2506.23625 (2025).
- <sup>34</sup>X.-F. Jiao, M.-Y. Zheng, Y.-H. Chen, B. Cao, X. Wang, Y. Liu, C.-A. Yang, X.-P. Xie, C.-Y. Lu, Z.-C. Niu, et al., "Electrically pumped ultrabright entangled photons on chip," arXiv preprint arXiv:2508.14566 (2025).
- <sup>35</sup>P. Kultavewuti, E. Y. Zhu, X. Xing, L. Qian, V. Pusino, M. Sorel, and J. S. Aitchison, "Polarization-entangled photon pair sources based on spontaneous four wave mixing assisted by polarization mode dispersion," Scientific reports 7, 5785 (2017).
- <sup>36</sup>F. Appas, F. Baboux, M. I. Amanti, A. Lemaítre, F. Boitier, E. Diamanti, and S. Ducci, "Flexible entanglement-distribution network with an algaas chip for secure communica-

- tions," npj Quantum Information 7, 118 (2021).
- <sup>37</sup>D. Kang, M. Kim, H. He, and A. S. Helmy, "Two polarization-entangled sources from the same semiconductor chip," Physical Review A **92**, 013821 (2015).
- <sup>38</sup>D. Zhu, L. Shao, M. Yu, R. Cheng, B. Desiatov, C. Xin, Y. Hu, J. Holzgrafe, S. Ghosh, A. Shams-Ansari, et al., "Integrated photonics on thin-film lithium niobate," Advances in Optics and Photonics 13, 242–352 (2021).
- <sup>39</sup>E. Meyer-Scott, N. Prasannan, C. Eigner, V. Quiring, J. M. Donohue, S. Barkhofen, and C. Silberhorn, "High-performance source of spectrally pure, polarization entangled photon pairs based on hybrid integrated-bulk optics," Optics Express 26, 32475–32490 (2018).
- <sup>40</sup>L. T. Weinbrenner, N. Prasannan, K. Hansenne, S. Denker, J. Sperling, B. Brecht, C. Silberhorn, and O. Gühne, "Certifying the topology of quantum networks: theory and experiment," Physical Review Letters 132, 240802 (2024).
- <sup>41</sup>Q.-C. Sun, Y.-F. Jiang, Y.-L. Mao, L.-X. You, W. Zhang, W.-J. Zhang, X. Jiang, T.-Y. Chen, H. Li, Y.-D. Huang, *et al.*, "Entanglement swapping over 100 km optical fiber with independent entangled photon-pair sources," Optica 4, 1214–1218 (2017).
- <sup>42</sup>S. I. Davis, R. Valivarthi, A. Cameron, C. Pena, S. Xie, L. Narvaez, N. Lauk, C. Li, K. Taylor, R. Youssef, *et al.*, "Entanglement swapping systems toward a quantum internet," arXiv preprint arXiv:2503.18906 (2025).
- <sup>43</sup>N. Brunner, D. Cavalcanti, S. Pironio, V. Scarani, and S. Wehner, "Bell nonlocality," Reviews of Modern Physics **86**, 419–478 (2014).
- <sup>44</sup>V. Scarani, H. Bechmann-Pasquinucci, N. J. Cerf, M. Dušek, N. Lütkenhaus, and M. Peev, "The security of practical quantum key distribution," Reviews of Modern Physics **81**, 1301–1350 (2009).
- <sup>45</sup>S. Wengerowsky, S. K. Joshi, F. Steinlechner, J. R. Zichi, B. Liu, T. Scheidl, S. M. Dobrovolskiy, R. v. d. Molen, J. W. Los, V. Zwiller, et al., "Passively stable distribution of polarisation entanglement over 192 km of deployed optical fibre," npj Quantum Information 6, 5 (2020).
- <sup>46</sup>P. Pathumsoot, T. Tansuwannont, N. Benchasattabuse, R. Satoh, M. Hajdušek, P. Chaiwongkhot, S. Suwanna, and R. Van Meter, "Boosting end-to-end entanglement fidelity in quantum repeater networks via hybridized strategies," in 2024 International Conference on Quantum Communications, Networking, and Computing (QCNC) (IEEE, 2024) pp. 49–56.
- <sup>47</sup>X. Shi, A. A. Baiju, X. Chen, S. S. Mohanraj, S. Wang, V. Dhyani, B. Shajilal, M. Zhao, R. Yang, Y. Li, *et al.*, "Squeezed light generation in periodically poled thin-film lithium niobate waveguides," arXiv preprint arXiv:2508.08599 (2025).
- <sup>48</sup>X. Liang, L. Fu, Q. Yu, Z. Xue, X. Shi, Y. Lu, H. Chen, B. Zhang, Y. Luo, Q. Hu, et al., "Efficient and broadband trident spot-size convertor for thin-film lithium niobate integrated device," IEEE Photonics Technology Letters **35**, 35–38 (2022).
- <sup>49</sup>N. Gisin, G. Ribordy, W. Tittel, and H. Zbinden, "Quantum cryptography," Reviews of modern physics **74**, 145 (2002).
- <sup>50</sup>V. Rodimin, K. Kravtsov, R. M. Chua, G. De Santis, A. Ponasenko, Y. Kurochkin, A. Ling, and J. A. Grieve, "Impact of polarization mode dispersion on entangled photon distribution," Physical Review A 112, 032620 (2025).
- <sup>51</sup>A. Miloshevsky, L. M. Cohen, K. V. Myilswamy, M. Alshowkan, S. Fatema, H.-H. Lu, A. M. Weiner, and J. M. Lukens, "Cmos photonic integrated source of broadband polarization-entangled photons," Optica Quantum 2, 254–259 (2024).
- <sup>52</sup>S. P. Neumann, A. Buchner, L. Bulla, M. Bohmann, and R. Ursin, "Continuous entanglement distribution over a transnational 248 km fiber link," Nature Communications 13,

6134 (2022).

- <sup>53</sup>R. Bedington, J. M. Arrazola, and A. Ling, "Progress in satellite quantum key distribution," npj Quantum Information 3, 30 (2017).
- <sup>54</sup>J. S. Sidhu, S. K. Joshi, M. Gündoğan, T. Brougham, D. Lowndes, L. Mazzarella, M. Krutzik, S. Mohapatra, D. Dequal, G. Vallone, P. Villoresi, A. Ling, T. Jennewein, M. Mohageg, J. G. Rarity, I. Fuentes, S. Pirandola, and D. K. L. Oi, "Advances in space quantum communications," IET Quantum Communication 2, 182–217 (2021).
- <sup>55</sup>X. Shi, S. S. Mohanraj, V. Dhyani, A. A. Baiju, S. Wang, J. Sun, L. Zhou, A. Paterova, V. Leong, and D. Zhu, "Efficient photon-pair generation in layer-poled lithium niobate nanophotonic waveguides," Light: Science & Applications 13, 282 (2024).